
Article:
Quindeau, Andy, Avci, Can O., Liu, Wenqing et al. (10 more authors) (2017) Tm3Fe5O12/Pt Heterostructures with Perpendicular Magnetic Anisotropy for Spintronic Applications. Advanced Electronic Materials. 1600376. ISSN: 2199-160X

https://doi.org/10.1002/aelm.201600376

$Tm_3Fe_5O_{12}$/Pt Heterostructures with Perpendicular Magnetic Anisotropy for Spintronic Applications

Andy Quindeau*[1], Can O. Avci[1], Wenqing Liu[2,3], Congli Sun[4], Maxwell Mann[1], Astera T. Tang[1], Mehmet C. Onbasli[1], David Bono[1], Paul M. Voyles[4], Geoffrey S. D. Beach[1] and Yongbing Xu,[2] Caroline A. Ross*[1]

[1]*Department of Materials Science and Engineering, Massachusetts Institute of Technology, Cambridge, Massachusetts 02139, USA*

[2] *Department of Electronics, University of York, York YO10 5DD, UK*

[3] *Department of Materials Science and Metallurgy, University of Cambridge, 27 Charles Babbage Road, Cambridge CB3 0FS, UK*

[4]*Department of Materials Science and Engineering, University of Wisconsin-Madison, Madison, Wisconsin 53706, USA*

* Correspondence: caross@mit.edu and quindeau@mit.edu

With recent developments in the field of spintronics, ferromagnetic insulator (FMI) thin films have emerged as an important component of spintronic devices. Yttrium iron garnet in particular is an excellent candidate for spin logic applications due to its low magnon damping and large spin wave propagation length. However, it has been a challenge to find FMI thin films with perpendicular magnetic anisotropy (PMA) which share these characteristics. Such materials could expand existing experimental approaches and enable the development of low dissipation

memory and logic devices based on spin orbit torques. In this work, we demonstrate robust PMA in strained ultra thin thulium iron garnet (TmIG) films of high structural quality down to a thickness of $5.6\ \mathrm{nm}$ which retain a magnetization close to bulk. Platinum deposited on TmIG possesses large spin Hall magnetoresistance (SMR), which indicates efficient spin transmission across the FMI/Pt interface, and SMR measurements are used to characterize the magnetic anisotropy of the TmIG. which has so far been inaccessible by means of standard methods.

Harnessing the electron's second fundamental property, its spin, is the basis of spintronic phenomena and devices[1]. These include recently discovered phenomena like the quantum anomalous Hall effect[2] in magnetic topological insulators[3], spin transfer torque[4,5] effects in nonmagnetic metal / ferromagnetic metal / oxide heterostructures and spin transfer torque (SOT) switching of ferromagnets[6,7], and ultimately of FMIs[8]. To realize novel circuit devices based on these effects a rich variety of specifically tailored magnetic materials has still to be developed. For instance, the study of exotic phenomena occurring at the boundary of topological insulators with ferromagnets requires the latter to be insulating, yet to retain magnetic properties including PMA.

One of the most prominent FMIs classes is that of iron garnets, of which the most well studied is $Y_3Fe_5O_{12}$ (YIG). The ultra low magnon damping characteristics[9] and magneto-optical properties[10,11] of YIG are well known. The former makes YIG a suitable candidate for spin wave logic[12] and signal transmitters[13] due to the extremely large

magnon decay length of several tens of millimeters. Epitaxial YIG thin films can, in principle, also possess PMA as a result of magnetization-lattice coupling[14] for thicknesses below $14\ \mathrm{nm}$[15,16], but the fabrication of YIG films with complete out-of-plane remanence remains elusive because of its low magnetocrystalline anisotropy and magnetoelastic coefficients. In contrast, 50 nm thick thulium iron garnet ($Tm_3Fe_5O_{12}$, TmIG), has been reported to show PMA[17,18] caused by magnetoelastic anisotropy when grown epitaxially on (111)-oriented gallium gadolinium garnet ($Gd_3Ga_5O_{12}$ or GGG)[19]. We recently demonstrated[8] reversible magnetization switching in 8 nm thick TmIG by utilizing SOT from an adjacent platinum layer, but a detailed structural and magnetic characterization of TmIG in the few-nm thickness regime is still lacking. In the present article, we provide a comprehensive description of the structural characteristics and magnetic properties of TmIG/GGG down to a thickness of $5.6\ \mathrm{nm}$. Furthermore we demonstrate that efficient spin transport can be achieved through the TmIG/Pt interface by measuring spin Hall magnetoresistance (SMR) in Pt. We exploit this method to measure the anisotropy field of the strained TmIG film electrically, which is inaccessible by conventional magnetometry measurements due to the dominant paramagnetic contribution of the GGG substrate. These results emphasize the potential of TmIG as a spintronic material.

Structural characterization of the TmIG films are summarized in Fig.1. With xray reflectometry (XRR) scans (not shown), we measured film thicknesses of PMA epitaxial TmIG down to $5.6\ \mathrm{nm}\ (\pm 0.1\ \mathrm{nm})$. To quantify the strain state of TmIG via XRD we measured a $19.7\ \mathrm{nm}$ thick TmIG film, since thinner films could not be resolved with enough intensity using high resolution XRD. The symmetric XRD spectra shown in

Fig.1a demonstrates a fully strained film with lattice spacing of $d_{(444)}^{TmIG,XRD} = 0.1769\ \mathrm{nm}$. Laue fringes around the TmIG peak underline the high quality of the thin layer. A reciprocal space map (Fig.1b) around the TmIG and GGG $(624)_+$ asymmetric peaks of the $19.7\ \mathrm{nm}$ thick TmIG sample confirms the coherent growth of the TmIG on the GGG substrate. The in-plane values for the (220) lattice spacing for both the TmIG film and the substrate are $d_{(220)}^{TmIG} = d_{(220)}^{GGG} = {}^{1}/_{q_x} = 0.4377\ \mathrm{nm}$, which is in very good agreement with literature values for GGG [20]. The out-of-plane lattice spacing value for the TmIG film in the RSM is $d_{(444)}^{TmIG,RSM} = {}^{1}/_{q_z} = 0.1768\ \mathrm{nm}$, close to that measured by symmetric XRD. The resulting distortion angle for the (111) direction compressed pseudo-cubic TmIG unit cell is $\beta = 90.77°$ (Fig.1d). We assume that, since the 19.7 nm thick film is fully strained to the substrate, thinner films are also fully strained. Temperature dependent measurements of the d_{444} lattice plane and angle of GGG and TmIG (Fig. 1c) reveal linear thermal expansion coefficients in the (111) direction of $\alpha_{L,GGG} = 14.1 \cdot 10^{-6}\ \mathrm{K}^{-1}$ and $\alpha_{L,TmIG} = 15.57 \cdot 10^{-6}\ \mathrm{K}^{-1}$ for the substrate and the film, respectively. Evidently, the lattice angle decreases with temperature, and by linear regression a complete loss of the strain state can be estimated at a temperature of above 2559 °C.

The surface morphology of the $19.7\ \mathrm{nm}$ thin TmIG film was measured via atomic force microscopy (AFM) (Fig.2a) and possesses a RMS roughness value of $1.5\ \mathrm{nm}$. Surface roughness values of thinner films, used for interface studies, were in the range of down to 0.2 nm. A high resolution image of the atom columns in the $(11\bar{2})$ direction is shown in Fig.1e. The yellow arrow indicates the interface between TmIG and the GGG substrate. There is no evidence of defects in the crystal structure of TmIG or at the

interface over the field of the images. Figure 1f shows HAADF STEM in the $(10\bar{1})$ direction and corresponding electron energy loss spectroscopy (EELS) line scans (Fig.1f) perpendicular to the interface, which evidently demonstrate that there is no interdiffusion of the respective elements in either of the garnet materials.

The magnetic properties of the TmIG were measured using magnetometry, MFM and XMCD. Fig. 2b shows an MFM image of the demagnetized $19.7\ \mathrm{nm}$ thin TmIG film. For the demagnetization process, the sample was placed in an alternating magnetic field that reversed its polarization with a frequency of 10 Hz and exponentially decreased its amplitude from 160 kA/m to 0 over a time period of 2 minutes. The domain pattern is typical for PMA materials without lateral anisotropy[21] and the area coverage of up- and down-magnetized domains is, as expected, approximately equal. Polar MOKE and vibrating sample magnetometry (VSM) measurements on the $5.6\ \mathrm{nm}$ thin TmIG film are shown in Fig.2c,d showing square hysteresis loops with coercivity of $300\ \mathrm{Oe}$. No hysteretic behavior was measurable in the plane direction, which suggests uniaxial anisotropy with easy axis along the surface normal. Based on the thickness derived from a XRR measurement, the saturation magnetization M_S for the $5.6\ \mathrm{nm}$ thick TmIG sample was estimated at around $100\ (\pm 1.5)\ {}^{\mathrm{emu}}/_{\mathrm{cm}^3}$. This value is in good agreement with data measured for bulk TmIG[19]. We found that the magnetization value does not change for a variety of different film thicknesses and possesses values between 90 and $100\ {}^{\mathrm{emu}}/_{\mathrm{cm}^3}$.

The magnetic anisotropy of the TmIG films includes contributions from magnetocrystalline, magnetoelastic and shape anisotropies. Room temperature values

for the first order cubic anisotropy constant K_1 and the magnetostriction coefficients λ_{111} and λ_{100} of bulk TmIG have been reported to be $-110\ {}^{\mathrm{kJ}}/_{\mathrm{m}^3} < K_1 < -58\ {}^{\mathrm{kJ}}/_{\mathrm{m}^3}$, $\lambda_{111} = -5.2 \cdot 10^{-6}$ and $\lambda_{001} = 1.4 \cdot 10^{-6}$ [19]. The uniaxial anisotropy K_u is the difference between the total magnetic energy when the magnetization is oriented in plane vs. out of plane, and can be written as

$K_u = E_{IP} - E_{OP} = -{}^{K_1}/_{12} + {}^{9}/_{8}\,\lambda_{111}c_{44}\left({}^{\pi}/_{2} - \alpha\right) - \left({}^{\mu_0}/_{2}\right)M_S{}^2$ [22].

where the magnetoelastic term includes the shear strain (related to the distortion angle β) and the shear modulus $c_{44} = 76.4\ \mathrm{GPa}$ [23], which is the value for YIG at room temperature (used as an estimate due to lag of elastic data for TmIG). This yields estimated boundaries for the expected uniaxial anisotropy in the range of $9.8\ {}^{\mathrm{kJ}}/_{\mathrm{m}^3} < K_u < 14.1\ {}^{\mathrm{kJ}}/_{\mathrm{m}^3}$, which indicates a strong easy axis out of the plane.

A detailed investigation of the element-specific magnetic structure of TmIG was conducted using XMCD at the Diamond Light Source, UK. It is already obvious from the XAS spectra that the circularly polarized X-ray beams yield significantly distinct spectra as a function of their respective helicity (blue lines vs. red lines). To isolate the XMCD signal from the XAS, we calculated the asymmetry of the absorption signal via: $I_{asy} = \frac{I_{\sigma^-} - I_{\sigma^+}}{I_{\sigma^-} + I_{\sigma^+}}$, where $I_{\sigma^\pm}$ are the TEY-XAS intensities for the respective helicities of the emitted light $\sigma^\pm$ (Fig.2e,f, lower half). As anticipated, the resulting spectra around the iron $L_{2,3}$ edges are consistent with antiferromagnetic coupling between Fe in the *a* (octahedral) and *d* (tetrahedral) sites in the garnet unit cell. The spectra around the $M_{4,5}$ edges of the

thulium atoms confirm that Tm is ferromagnetically coupled to the *a* site Fe ions[24]. As anticipated from prior literature on bulk TmIG [25], temperature-dependent measurements (not published here) have confirmed that no compensation point was found for TmIG strained thin films in the temperature range between $1.5\ \mathrm{K}$ and $300\ \mathrm{K}$.

Next, we want to exploit the spintronic properties of TmIG as an active component to measure the magnetic total anisotropy of a Pt$(5\ \mathrm{nm})$/TmIG$(8\ \mathrm{nm})$ bilayer. We note that this type characterization is a convenient way of neglecting the paramagnetic background of the GGG substrate. We demonstrate our results on a Hall bar structure different from the device that we have used to demonstrate reversible magnetization switching[8].

The heavy metal Pt is well suited to convert charge current into a pure spin current and vice versa, thanks to its large spin-orbit coupling combined with low resistivity. Recently, it has been discovered that Pt in contact with a FMI can show magnetoresistance due to the interaction of the SHE-induced spin accumulation at the Pt/FMI interface with the magnetization ($\mathbf{m}$) of a FMI[26]. This so-called spin Hall magnetoresistance (SMR) increases (decreases) the longitudinal resistance when the spin current is absorbed (reflected) by the FMI. The spin current transmission across interfaces is dictated by the spin mixing conductance concept, which parameterize the interface transparency to the spin current and which is crucial for SMR[27,28], spin Seebeck effect[29], and spin-orbit torque[30] studies. The additional SMR contribution to the longitudinal resistance scales with $\Delta R \propto \mathbf{m}_{\boldsymbol{y}}^{\mathbf{2}}$ assuming charge current flow along x, and z being the direction normal to the layer plane. The SMR also has a transverse (Hall resistance) component with symmetry $R_{SMR} \propto \mathbf{m}_{\boldsymbol{x}}\mathbf{m}_{\boldsymbol{y}}$ analogous to the planar Hall effect in ferromagnets.

Additionally, it has been theorized[31] and measured[32] that the imaginary part of the spin mixing conductance gives rise to a transverse anomalous Hall-like signal with symmetry $R_{AHE} \propto \mathbf{m_z}$ with much lower amplitude compared to R_{SMR}. By combining these and the ordinary Hall effect of Pt we can write the expected angular symmetry of the transverse Hall effect resistance (R_H) as follows:

$$R_H = R_{SMR} \sin^2\theta \sin 2\varphi + R_{AHE} \cos\theta + R_{OHE} H_z \quad \textbf{(1)}$$

where θ and φ are the polar and azimuthal angles of $\mathbf{m}$, respectively, as depicted in Fig.3a, and R_{OHE} is the ordinary Hall resistance due to an out-of-plane field H_z. To characterize the SMR, AHE and OHE in Pt/TmIG bilayers we have injected an ac current of amplitude $I_{ac} = 1.8$ mA (rms) with frequency $\omega/2\pi = 3678$ Hz, and measured the first harmonic Hall voltage as schematized in Fig.3a. This is equivalent to standard dc measurements but with much higher signal-to-noise ratio. The inset shows the optical microscope image of the device utilized throughout this section.

Figure 3b depicts the Hall resistance for an out-of-plane field sweep. We recognize the AHE contribution following $\mathbf{m_z}$ which reverses between up and down states at the coercive field of ≈ 11.9 kA/m. The linear slope independent of $\mathbf{m}$ direction (orange dashed lines) characterizes itself as R_{OHE}. This measurement shows that $\mathbf{m}$ has 100% remanence, and sharp transitions between up and down states suggest low pinning and efficient propagation of domain walls, assuming that the reversal is mediated by domain nucleation and propagation.

Figure 3c exhibits R_H for in-plane field sweep at various φ. In this geometry R_{OHE} does not contribute to the signal, and thus we can characterize R_{SMR} by analyzing the angular

dependence of the signal at high fields where R_{AHE} becomes negligibly small. The specific U-shape of the signal is due to coherent rotation of the magnetization towards the layer plane at higher *H*. We find that $H \geq 19.9$ kA/m is necessary to saturate $\mathbf{m}$ fully in-plane, which gives an indication of the effective perpendicular magnetic anisotropy field (H_K) of TmIG. Macrospin simulations (not shown) suggest that for this measurement $H_K \cong 198.9 \pm 15.9\,\mathrm{kA/m}$, which is large enough for use as potential future memory devices. We note that the features around $H = 0$ A/m are due to R_{AHE} since $\mathbf{m}$ switches between up and down states due to a small unintentional out-of-plane component of the field.

With the values for H_K and M_S, the total anisotropy energy at room temperature was calculated to be $K_u = 11.88\ {}^{\mathrm{kJ}}/_{\mathrm{m}^3}$ and lies thus within the boundary of the above estimated value. We can calculate the contribution of the magnetoelastic anisotropy to be in the range between $-1.5\ {}^{\mathrm{kJ}}/_{\mathrm{m}^3} < K_{ME} < 2.871\ {}^{\mathrm{kJ}}/_{\mathrm{m}^3}$. Based on this finding, we conclude that the contribution to the total magnetic anisotropy is mainly governed by the crystallographic anisotropy.

In Fig.3d we plot R_H obtained at $H = \pm 318.3$ kA/m for different φ. We fit the data by using Eq.1 and obtain $R_{SMR} = 8.2$ mΩ. By transforming R_{SMR} and R_{AHE} into resistivity, taking $\rho_{xx}^{Pt} = 40$ μΩcm as measured on the same device, assuming $\theta_{SH} = 0.08$ for Pt and taking the spin diffusion length to be $\lambda_{Pt} = 1.4$ nm, we estimate the real and imaginary part of the spin mixing conductance as $G_r^{\uparrow\downarrow} = 1.3 \times 10^{14}$ $\Omega^{-1}\mathrm{m}^{-2}$ and $G_i^{\uparrow\downarrow} = 4.8 \times 10^{12}$ $\Omega^{-1}\mathrm{m}^{-2}$, respectively. These compare well with commonly accepted values for Pt/YIG and suggest highly efficient transmission of spin current across Pt/TmIG interface.

We now discuss the effect of temperature rise due to Joule heating on H_K. Figure 3e shows R_H taken at $\varphi_H = +\pi/4$ with applied current varying between 1.8 and 10.2 mA, corresponding to $j = 4.8 \cdot 10^{10}$ and $2.72 \cdot 10^{11}$A/m^2, respectively. We observe that, although the SMR amplitude remains nearly the same, the field required to saturate $\mathbf{m}$ fully in-plane decreases systematically, as well as the coercivity. We attribute this behavior to H_K decreasing as a function of increasing temperature due to Joule heating. In Fig.3f we plot H_K as a function of I_{app} (purple squares). We observe that when I_{app} is increased from 1.8 to 10.2 mA, H_K decreases more than 50%. To further support this hypothesis we measure the device resistance (R) as a function of I_{app} (red circles). The fit to the data (black dashed line) shows that R increases quadratically as a function of I_{app} as expected from Joule heating-induced temperature rise ($T \propto I_{app}^2 R$). From this behavior we learn that the magnetic anisotropy of TmIG evidently shows strong temperature dependence, whereas M_S stays almost constant. By applying a current of 10 mA, the distortion angle changes from $\alpha_{RT} = 90.77°$ at room temperature to $\alpha_{85°C} = 90.75°$ at 85 °C due to the difference in thermal expansion coefficients of the bilayer system. This leads to a change in the strain state of 0.03%, which can thus not account for the large change of the total anisotropy energy measured in this system, given the small contribution of magnetoelastic anisotropy that was estimated before.

In summary, we characterized thin film ferrimagnetic garnet TmIG that possesses robust perpendicular magnetic anisotropy under tensile strain in (111) direction down to a thickness of 5.6 nm. We showed strong spin mixing conductance at the interface between Pt and TmIG. This emphasizes the usability of this material system for

spintronic experiments that require FMI layers with PMA. By exploiting the SMR of the TmIG/Pt bilayer, we directly measured the anisotropy field of TmIG. We propose that the high spin mixing conductance and specific magnetic parameters found in this material are promising starting points for future studies on the quantum anomalous Hall effect, which might potentially increase the observation temperature of dissipationless chiral edge states in magnetic topological insulators by proximity effect. We further found that a small temperature induced change in the strain state with little magnetoelastic contribution can only marginally account for the strong temperature variation of the total anisotropy K_u, which will be subject to more specific investigation.

Methods

TmIG thin films were deposited using pulsed laser deposition (PLD) on single-crystal GGG substrates with (111) orientation. The stoichiometric target used during the deposition process was made in house by mixing powders of Tm and Fe oxides in the appropriate weight ratios, and then calcining the mix at 1150 °C for 5 hours, cold-pressing it into a target, and sintering the target at 1350 °C for 10 hours. The stoichiometry of the target was confirmed by wavelength dispersion spectroscopy conducted at various locations on the target surface. To ensure epitaxial growth conditions during the PLD process, a substrate temperature of $650\ °\mathrm{C}$, a laser fluence of $2\ {}^{\mathrm{J}}/_{\mathrm{cm}^2}$, a laser repetition rate of $10\ \mathrm{Hz}$ and a O_2 pressure of $200\ \mathrm{mTorr}$ were applied.

After the deposition the substrate was cooled down to room temperature in $200\ \mathrm{mTorr}$ O_2 at a rate of $2\ {}^{\mathrm{K}}/_{\mathrm{min}}$. We found that an additional annealing step was not necessary,

but the slow cooling step after deposition was crucial in order to obtain the best quality films.

Cross-sectional TEM imaging of the structure was carried out using a FEI TITAN (S)TEM with a CEOS probe aberration corrector operated at $200\,\mathrm{kV}$, which achieves a spatial resolution of less than $0.8\,\text{Å}$. The use of a HAADF detector in STEM mode allowed us to record elastic, thermal diffuse scattering events that are proportional to Z^2 and thus determine the position of atom columns or individual atoms as brightness contrast proportional to their atomic number. The TEM lamellas were prepared using a focused ion beam (Zeiss Auriga cross beam system).

X-ray absorption spectra (XAS) were collected at the Fe $L_{2,3}$ and Tm $M_{4,5}$ absorption edges by total electron yield (TEY) measurements (Fig.2e,f, upper half), assisted by an ultra thin $(3\,nm)$ Au capping layer on top of the TmIG. Oppositely circular polarized X-rays with 100% degree of polarization were used successively to resolve XMCD signals from the respective elements. The light-helicity was switched in a saturating magnetic field of $6\,T$, which was applied normal to the film plane and in parallel with the incident beam.

To study the properties of TmIG as a spinterface material, we sputtered $5\,\mathrm{nm}$ Pt on top of a $8\,\mathrm{nm}$ thin TmIG film. We then defined $16 \times 7\,\mu\mathrm{m}^2$ sized Hall crosses (Fig.3a) in resist by a photolithography process and used ion milling to create Pt/TmIG mesa structures. Using an etching- instead of a liftoff process improved the quality of the Pt/TmIG interface by avoiding residual resist layers between the TmIG and the Pt.

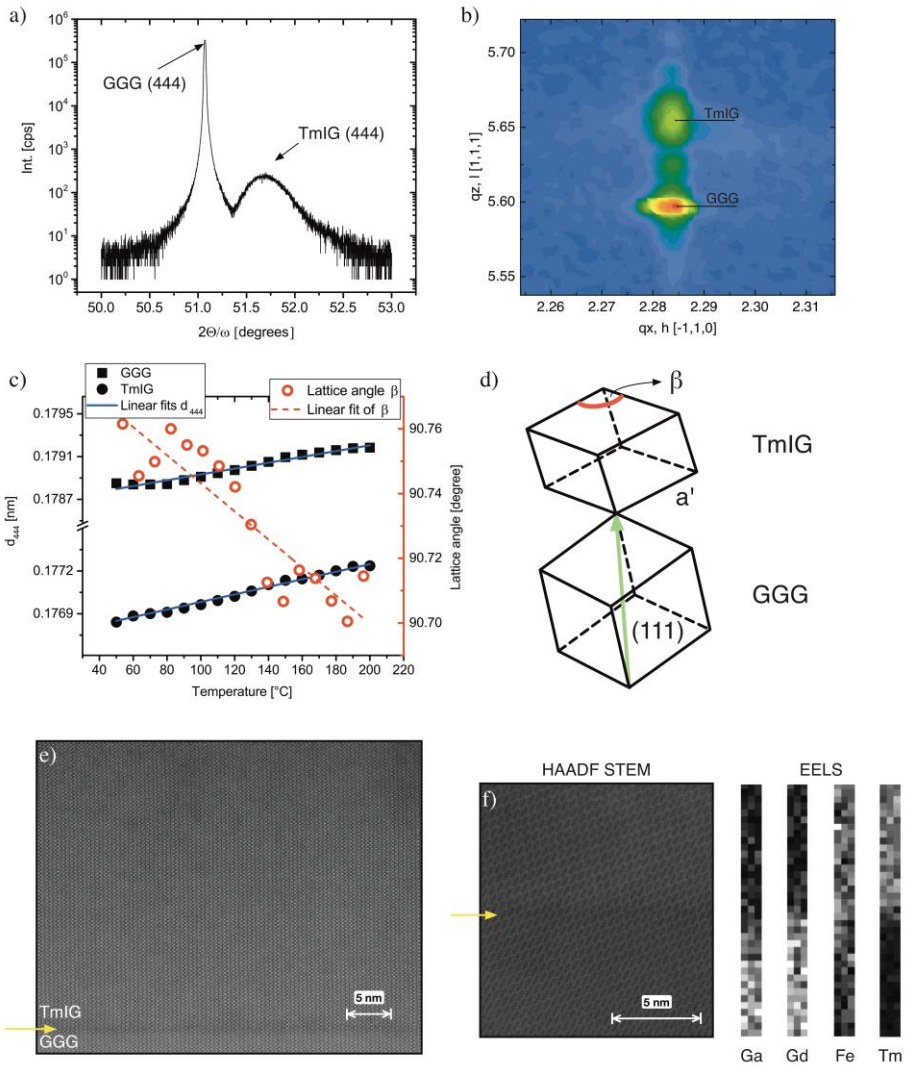

Figure 1 - Structural characterization of TmIG. a), XRD symmetric scan of the TmIG(19.7 nm)/GGG sample around the (444) peak. b), Reciprocal space map of the asymmetric $(624)_+$ diffraction peaks of the substrate GGG (lower peak) and the film (upper peak). c) Temperature evolution of the TmIG and GGG d_{444} lattice parameters and of the resulting lattice angle β. d), Sketch of the two adjacent pseudo cubic unit cells of TmIG and GGG at the interface. The deformation of the TmIG unit cell is exaggerated to visualize the lattice distortion angle α. e)+f) HAADF STEM images of the TmIG/GGG

structure at the interface in the $(10\bar{2})$- direction (e) and $(10\bar{1})$- direction (f). EELS line scans at the interface show the distribution of Ga, Gd, Fe, and Tm atoms as black-white contrast.

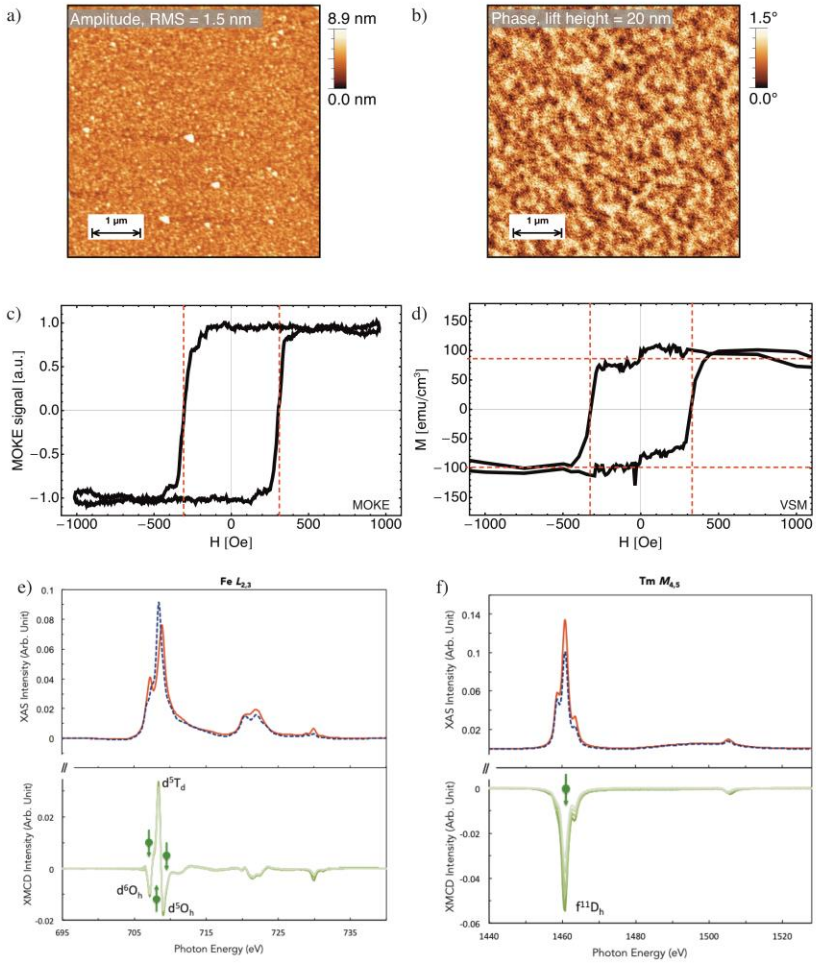

Figure 2 - Magnetic characterization of TmIG thin films. a)+b), Amplitude- and phase images of a MFM scan on the TmIG thin film. The RMS value for the surface roughness is $RMS = 1.5\,\mathrm{nm}$ and characteristic stripe domains of the out-of-plane demagnetized film shown in the phase image possess a feature size in the $1\,\mu\mathrm{m}$ – range. c), Polar MOKE signal versus applied out-of-plane magnetic field for the 5.6 nm thick TmIG film. d), Vibrating sample magnetometer measurement on the same film with field applied normal to the sample plane. e)+f), The XAS and XMCD asymmetric intensity signals for

the $L_{2,3}$ edge of Fe and the $L_{4,5}$ edge of Tm, respectively. The insets in the upper figures show the XMCD signals as a function of the (constant) magnetic field applied normal to the plane. The arrows in the lower figures correspond to the magnetization direction at the respective energy peak, pointing up (down) for positive (negative) XMCD signal.

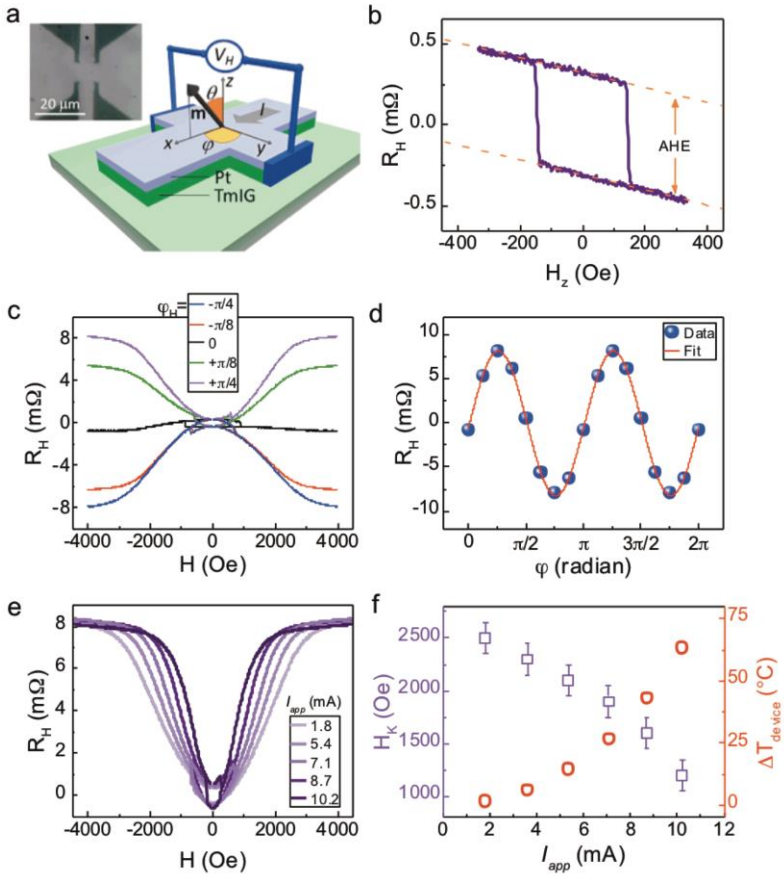

Figure 3 - SMR measurements on a TmIG/Pt bilayer device. a), Schematics of the electrical measurements and the definition of coordinate axes and angles. Upper left: optical image of the measured device. b), Hall resistance as a function of an out-of-plane field showing the anomalous Hall (two levels) and ordinary Hall (linear slope) contributions. c), Hall resistance as a function of an in-plane field sweep applied at different angles φ. d), In-plane angular variation of the Hall resistance recorded at

$H = \pm 318\ {}^{\mathrm{kA}}/_{\mathrm{m}}$. Fit according to Eq.1 shows that the signal is purely driven by the SMR. e), Variation of Hall resistance as a function of applied current. Different shapes suggest that the effective anisotropy field depends on I_{app} henceforth on the Joule heating. f), calculated PMA field and the variation of the device resistance as a function of I_{app}. We see that the increase of the resistance due to Joule heating correlates with the decrease in H_K.

References

[1] C. Chappert, A. Fert, F. N. Van Dau, *Nat. Mater.* **2007**, *6*, 813.

[2] C.-Z. Chang, J. Zhang, X. Feng, J. Shen, Z. Zhang, M. Guo, K. Li, Y. Ou, P. Wei, L.-L. Wang, Z.-Q. Ji, Y. Feng, S. Ji, X. Chen, J. Jia, X. Dai, Z. Fang, S.-C. Zhang, K. He, Y. Wang, L. Lu, X.-C. Ma, Q.-K. Xue, *Science (80-.).* **2013**, *340*, 167.

[3] Y. Ando, *J. Phys. Soc. Japan* **2013**, *82*, 1.

[4] J. C. C. Slonczewski, *J. Magn. Magn. Mater.* **1996**, *159*, L1.

[5] L. Berger, *Phys. Rev. B* **1996**, *54*, 9353.

[6] I. M. Miron, K. Garello, G. Gaudin, P. J. Zermatten, M. V., Costache, Stéphane Auffret, Sebastien Bandiera, Bernard Rodmacq, Alain Schuhl, P. Gambardella, *Nature* **2011**, *476*, 189.

[7] L. Q. Liu, C.-F. Pai, Y. Li, H. W. Tseng, D. C. Ralph, R. A. Buhrman, *Science (80-.).* **2012**, *336*, 555.

[8] C. O. Avci, A. Quindeau, C.-F. Pai, M. Mann, L. Caretta, A. S. Tang, M. C. Onbasli, C. A. Ross, G. S. D. Beach, *unpublished* **2016**.

[9] C. Hauser, T. Richter, N. Homonnay, C. Eisenschmidt, H. Deniz, D. Hesse, S.

Ebbinghaus, G. Schmidt, N. Weinberg, *Sci. Rep.* **2016**, *6*, 1.

[10] Y. Shoji, T. Mizumoto, H. Yokoi, I. W. Hsieh, R. M. Osgood, *Appl. Phys. Lett.* **2008**, *92*, DOI 10.1063/1.2884855.

[11] B. J. H. Stadler, T. Mizumoto, *IEEE Photonics J.* **2014**, *6*, DOI 10.1109/JPHOT.2013.2293618.

[12] T. Schneider, A. A. Serga, B. Leven, B. Hillebrands, R. L. Stamps, M. P. Kostylev, *Appl. Phys. Lett.* **2008**, *92*, DOI 10.1063/1.2834714.

[13] Y. Kajiwara, K. Harii, S. Takahashi, J. Ohe, K. Uchida, M. Mizuguchi, H. Umezawa, H. Kawai, K. Ando, K. Takanashi, S. Maekawa, E. Saitoh, *Nature* **2010**, *464*, 262.

[14] H. Wang, C. Du, P. C. Hammel, F. Yang, *Phys. Rev. B* **2014**, *89*, 134404.

[15] E. Popova, N. Keller, F. Gendron, M. Guyot, M. C. Brianso, Y. Dumond, M. Tessier, *J. Appl. Phys.* **2001**, *90*, 1422.

[16] E. Popova, N. Keller, F. Gendron, L. Thomas, M.-C. C. Brianso, M. Guyot, M. Tessier, S. S. P. Parkin, *J. Vac. Sci. Technol. A Vacuum, Surfaces, Film.* **2001**, *19*, 2567.

[17] M. Kubota, A. Tsukazaki, F. Kagawa, K. Shibuya, Y. Tokunaga, M. Kawasaki, Y. Tokura, K. Shibuyay, Y. Tokunaga, M. Kawasaki, Y. Tokura, *Appl. Phys. Express* **2012**, *5*, 103002.

[18] M. Kubota, K. Shibuya, Y. Tokunaga, F. Kagawa, a. Tsukazaki, Y. Tokura, M. Kawasaki, *J. Magn. Magn. Mater.* **2013**, *339*, 63.

[19] A. Paoletti, *Physics Of Magnetic Garnets*, North-Holland Publishing Company, Amsterdam - New York - Oxford, **1978**.

[20] H. Sawada, *J. Solid State Chem.* **1997**, *132*, 300.

[21] A. Hubert, R. Schäfer, in *Magn. Domains*, Springer, New York, **1998**, pp. 500–507.

[22] D. H. Kim, N. M. Aimon, L. Bi, J. M. Florez, G. F. Dionne, C. a Ross, *J. Phys. Condens. Matter* **2013**, *25*, 026002.

[23] Y. A. Burenkov, S. P. Nikanorov, *Magn. Ferroelectr.* **2002**, *44*, 318.

[24] W. Meyer, W. Sturhahn, E. Gerdau, *Hyperfine Interact.* **1994**, *94*, 2059.

[25] G. F. Dionne, P. F. Tumelty, *J. Appl. Phys.* **1979**, *50*, 8257.

[26] H. Nakayama, M. Althammer, Y. T. Chen, K. Uchida, Y. Kajiwara, D. Kikuchi, T. Ohtani, S. Geprags, M. Opel, S. Takahashi, R. Gross, G. E. W. Bauer, S. T. B. Goennenwein, E. Saitoh, *Phys. Rev. Lett.* **2013**, *110*, 206601.

[27] M. Weiler, M. Althammer, M. Schreier, J. Lotze, M. Pernpeintner, S. Meyer, H. Huebl, R. Gross, A. Kamra, J. Xiao, Y. T. Chen, H. J. Jiao, G. E. W. Bauer, S. T. B. Goennenwein, *Phys. Rev. Lett.* **2013**, *111*, 176601.

[28] N. Vlietstra, J. Shan, V. Castel, B. J. van Wees, J. Ben Youssef, *Phys. Rev. B* **2013**, *87*, 184421.

[29] K. I. Uchida, H. Adachi, T. Ota, H. Nakayama, S. Maekawa, E. Saitoh, *Appl. Phys. Lett.* **2010**, *97*, 18.

[30] C. F. Pai, Y. X. Ou, L. H. Vilela-Leao, D. C. Ralph, R. A. Buhrman, *Phys. Rev. B* **2015**, *92*, 64426.

[31] Y. T. Chen, S. Takahashi, H. Nakayama, M. Althammer, S. T. B. Goennenwein, E. Saitoh, G. E. W. Bauer, *Phys. Rev. B* **2013**, *87*, 144411.

[32] S. Meyer, R. Schlitz, S. Geprags, M. Opel, H. Huebl, R. Gross, S. T. B. Goennenwein, *Appl. Phys. Lett.* **2015**, *106*, 132402.

Acknowledgements

The authors acknowledge support from C-SPIN, one of the six SRC STARnet Centers sponsored by MARCO and DARPA. A.Q. acknowledges funding from the Max Planck Society and the Deutsche Forschungsgemeinschaft (DFG, German Research Foundation).